View metadata, citation and similar papers at core.ac.uk

brought to you by CORE

provided by UPCommons. Portal del coneixement obert de la UPC

Journal Name

ARTICLE

V_2O_x-Based Hole-Selective Contacts for c-Si Interdigitated Back-Contacted Solar Cells

Received 00th January 20xx,
Accepted 00th January 20xx

DOI: 10.1039/x0xx00000x

www.rsc.org/

Gerard Masmitjà,*[a] Luís G. Gerling,[a] Pablo Ortega,[a] Joaquim Puigdollers,[a] Isidro Martín,[a] Cristóbal Voz[a] and Ramón Alcubilla[a]

Over the last few years, transition metal oxide layers have been proposed as selective contacts both for electrons and holes and successfully applied to silicon solar cells. However, better published results need the use of both a thin and high quality intrinsic amorphous Si layer and TCO (Transparent Conductive Oxide) films. In this work, we explore the use of vanadium suboxide (V_2O_x) capped with a thin Ni layer as a hole transport layer trying to avoid both the intrinsic amorphous silicon layer and the TCO contact layer. Obtained figures of merit for Ni/V_2O_x/c-Si(n) test samples are saturation current densities of 175 fAcm^{-2} and specific contact resistance below 115 mΩcm^2 on 40 nm thick V_2O_x layers. Finally, the Ni/V_2O_x stack is used with an interdigitated back-contacted c-Si(n) solar cell architecture fully fabricated at low temperatures. An open circuit voltage, a short circuit current and a fill factor of 656 mV, 40.7 mAcm^{-2} and 74.0% are achieved, respectively, leading to a power conversion efficiency of 19.7%. These results confirm the high potential of Ni/V_2O_x stacks as hole-selective contacts on crystalline silicon photovoltaics.

Introduction

Crystalline silicon-based (c-Si) solar cells currently dominate the photovoltaic market, it is a mature technology where most research efforts are concentrated on maximizing efficiency and lowering processing costs. The last record[1] on photovoltaic conversion efficiency has been achieved by interdigitated back-contacted (IBC) solar cells structures. IBC solar cell is an old but attractive concept, which avoids shadow losses at the front surface.[2] This is accomplished by placing both electron and hole-selective contacts at the rear side of the device. One important advantage of this structure is the simplification of the passivation and antireflection scheme on the front side design, which is fully decoupled from the rear side strategy. So, the rear side can be optimized for an efficient separation/extraction of photogenerated carriers to the corresponding electrode. Although, high efficiency is routinely achieved on lab and industrial IBC cells, room for improvements exists by lowering processing temperatures and/or substitute toxic and flammable dopant gas precursors. In this way, research on dopant-free solar cells, where carrier selectivity[3] is achieved by alternative semiconductor materials, is an emerging research topic,[4] including organic polymers,[5] alkaline salts [6] and transition metal oxides (TMOs).[7]

Transition metal oxides are wide band gap (E_{gap} > 3 eV) semiconductors with a large range of work functions (3 – 7 eV) exhibiting n or p-type conductivity, offering a broad variety of optoelectronic properties.[8] Best known TMOs include molybdenum oxide MoO_x as hole transport layer (HTL) and titanium oxide TiO_x as electron transport layer (ETL), both frequently used in organic electronic devices.[8, 9] Where they are deposited by low-temperature and/or vacuum-free techniques, including solution-based processes. Their work function and conductivity are highly tuneable based on their oxygen content, which not only offers flexibility but also makes them highly sensitive to redox environments and surface chemistry.[10] For solar cells based on c-Si absorbers, high work function (> 5 eV) TMOs such as molybdenum oxide MoO_x, tungsten oxide WO_x and vanadium oxide V_2O_x can perform as efficient HTL films by promoting either an inversion layer on c-Si(n) or an accumulation layer on c-Si(p).[11,12]

Table 1 lists the latest results using high work function TMOs as HTL on c-Si solar cells. The preferred method for TMO-HTL film deposition is thermal evaporation, with MoO_x being the most reported material. Power conversion efficiencies of 18.8%,[13] 19.4%[14] and up to 22.5%[15] have been achieved on c-Si(n) devices, while an efficiency of 20.4% was reported for c-Si(p).[16] Additionally, V_2O_x and WO_x films are emerging alternatives yielding promising cell efficiencies of 18.3%[17] and 17.9%,[17] respectively, on n-type substrates. These results were achieved using a vertical solar cell structure with both surfaces contacted (conventional solar cells). Regarding IBC structures, several groups have reported recently conversion efficiencies of 15.4% (MoO_x),[18] 16.6% (V_2O_x)[19] and 12.4% (WO_x)[19] for c-Si(n) substrates. Generally speaking, the best results are achieved using a very thin intrinsic hydrogenated amorphous silicon, a-Si:H(i), passivation interlayer, which increases the complexity of

[a] Department of Electronic Engineering, Universitat Politècnica de Catalunya (UPC), c/ Jordi Girona 1-3, Modulo C-4, 08034 Barcelona, Spain. E-mail: gerard.masmitja@upc.edu

† Electronic Supplementary Information (ESI) available: Additional *I-V* curve, XPS measurements, HR-TEM image and EELS line scan. See DOI: 10.1039/x0xx00000x

Please do not adjust margins

Please do not adjust margins

Table 1. Best solar cells efficiencies fabricated on crystalline silicon using transition metal oxides acting as hole transport layer. All the solar cells are fabricated on n-type c-Si except for ref. 16, which is based on p-type c-Si. All a-Si:H films have been deposited by PECVD, whereas V_2O_x, MoO_x, WO_x, LiF_x and Cs_2CO_3 films have been thermally evaporated.

Institution	Ref.	Hole transport layer	Electron transport layer	Area (cm^2)	V_{oc} (mV)	J_{sc} ($mAcm^{-2}$)	FF (%)	Eff. (%)
Conventional solar cells								
UC & EPFL	[13]	a-Si:H(i)/MoO_x	a-Si:H(i)/a-Si:H(n)	4	711	39.4	67.2	18.8
UC, ANU & EPFL	[14]	a-Si:H(i)/MoO_x	a-Si:H(i)/LiF_x	4	716	37.1	73.1	19.4
EPFL & CSEM	[15]	a-Si:H(i)/MoO_x	a-Si:H(i)/a-Si:H(n)	4	725	38.6	80.4	22.5
		V_2O_x			606	34.4	75.3	15.7
UPC	[12]	MoO_x	a-SiC_x(n) DopLa [a)]	1	581	34.1	68.6	13.6
		WO_x			577	33.3	65.0	12.5
		a-Si:H(i)/MoO_x			710	33.4	80.0	19.0
Fraunhofer ISE	[17]	a-Si:H(i)/WO_x	a-Si:H(i)/a-Si:H(n)	4	685	33.8	78.0	17.9
		V_2O_x			684	34.0	79.0	18.3
ANU	[16]	MoO_x	P diffusion	4	658	39.8	77.8	20.4
Interdigitated back-contacted solar cells								
UNIST	[18]	MoO_x	LiF_x	1	561	36.8	74.6	15.4
		V_2O_x			610	38.8	70.0	16.6
SYSU & CCZU	[19]	MoO_x	Cs_2CO_3	4	594	38.4	66.1	15.1
		WO_x			539	37.7	61.3	12.4
UPC	**TW [b)]**	**V_2O_x**	**a-SiC_x(n) DopLa [a)]**	**9**	**656**	**40.7**	**74.0**	**19.7**

[a)]DopLa: Doped by Laser; [b)]TW: This Work

the final devices,[20,21] while only moderate open circuit voltages (V_{oc} ~ 600 mV) have been reported to date with bare TMO/c-Si heterojunctions. Recently, we demonstrated the surface passivation quality achieved by V_2O_x on c-Si(n) obtaining V_{oc} values above 610 mV in a conventional geometry, 20 – 30 mV more than using WO_x and MoO_x layers.[12] Also recently, excellent V_{oc} values around 680 mV have been achieved on c-Si(n) substrates.[17] Therefore, V_2O_x films seem to be a good candidate to form HTL regions on c-Si(n) solar cells.

In this work, we report on surface passivation and carrier selectivity of thermally evaporated V_2O_x films, as well as the impact of metal capping layer in the electrical contact performance. We demonstrate that Ni/V_2O_x/Si heterojunctions provide both a high level of carrier selectivity and low contact resistances on c-Si(n) substrates. Moreover, long-term and temperature stability of initial electrical properties are also analysed. Finally, this selective contact scheme is applied to an IBC c-Si(n) solar cell architecture, achieving a conversion efficiency of 19.7% on a 9 cm^2 device which favourably compares with those reported (see Table 1). It is also remarkable the high stable open circuit voltage of 656 mV reached in the final devices without additional passivation layer, i.e. a-Si:H(i).

Results and discussion

Surface passivation can be characterized in terms of an interface recombination velocity (S) or alternatively by means of recombination current density (J_0). The former parameter is more suitable for passivation dielectric layers, whereas the last is applied to selective contacts such as homo and heterojunctions. Independently of the type of surface, recombination can be evaluated by the so-called implied open circuit voltage iV_{oc} parameter,[22] the higher iV_{oc} value the lower recombination inside the device considering both bulk and surface recombination. All foregoing parameters can be obtained by effective lifetime (τ_{eff}) measurements using the quasi-steady-state photoconductance (QSS-PC) technique.[22]

The recombination current density of V_2O_x films (J_{0HTL}) was measured for different layer thicknesses (15, 30 and 60 nm) using asymmetrical samples (see the inset of Fig. 1d). In these samples, the front and rear sides were covered, respectively, with a V_2O_x layer and a dielectric passivating stack. In order to discriminate the recombination contribution of the selective contact in lifetime measurements, a well-passivated rear surface is necessary, i.e. a low rear surface recombination velocity (S_R). Layers like aluminium oxide Al_2O_3 deposited by atomic layer deposition (ALD)[23,24] or amorphous silicon carbide films a-SiC_x(n)[25] deposited by plasma-enhanced chemical vapour deposition (PECVD) meet that passivation requirements. For instance, the surface recombination velocity using ALD Al_2O_3 films can be as low as ~0.5 cms^{-1}, which corresponds to τ_{eff} values > 15 ms (at $\Delta n = 10^{15}$ cm^{-3}), as seen in the inset of Fig. 1a. Consequently, the J_{0HTL} parameter can be calculated as follows

$$\frac{1}{\tau_{eff}} - \frac{1}{\tau_{in}} = \frac{S_R}{W} + \frac{J_{0HTL}(N_D+\Delta n)}{q n_i^2 W} \cong \frac{J_{0HTL}(N_D+\Delta n)}{q n_i^2 W} \quad (1)$$

where w is the thickness of the wafer (280 µm), q is the elementary charge, n_i is the silicon intrinsic carrier concentration (n_i = 8.56×10^9 cm^{-3} at 25 °C), Δn is the carrier excess density and τ_{in} is the intrinsic bulk lifetime (Auger and radiative mechanisms).[26] Notice that the bulk Shockley-Read-Hall recombination mechanism has not been considered due to that high quality FZ c-Si used as substrate. From eqn (1) we can directly extract J_{0HTL} values for different V_2O_x thicknesses considering the slopes of $1/\tau_{eff}$ - $1/\tau_{in}$ versus Δn curves shown in Fig. 1a. Similar results were obtained independently of V_2O_x thickness yielding J_{0HTL} and iV_{oc} values of 175 ± 10 $fAcm^{-2}$ and 675 ± 5 mV respectively, in accordance with the state-of-the-art

Please do not adjust margins

related to this material.[17] In spite of the initial good J_{0HTL} and iV_{oc} results, surface passivation degrades with time as can be deduced from the strong drop in τ_{eff} shown in Fig. 1b. This might be due to a reduction of the material work function by chemical reaction of the samples with air (water and oxygen species),[27,28] weakening the induced p-type inversion region beneath the contacts and increasing local recombination, i.e. lower τ_{eff} values.

In order to mimic a final contacted solar cell, we explore the use of a nickel metal layer, which have a metal work function (ϕ_M) of ~5.4 eV, as capping material in a similar way as is reported in ref. 11 where palladium (ϕ_M ~5.6 eV) was used over MoO_x films. In order to allow reliable QSS-PC measurements Ni thickness is kept under 10 nm (in our case ~5 nm thick). This is mandatory to guarantee both, that the metal conductivity does not saturate the lifetime measurement system and enough light is transmitted into the silicon substrate. Fig. 1c shows the normalized iV_{oc} to the initial value (iV_{oc}^n) as a function of time when a thin nickel layer is deposited over 40 nm thick V_2O_x films. Samples with the metal capping exhibit a much better long-term surface passivation stability, pointing out that the Ni layer is thick enough to block the reaction of air chemical species with the V_2O_x films. In addition, Fig. 1d shows the evolution of the iV_{oc}^n parameter for accumulative 10 min annealings in forming gas at different temperatures. The Ni/V_2O_x films seem to be stable in temperature, from a surface passivation point of view, up to 300 °C without apparent degradation. These results demonstrate a great passivation stability and sufficient thermal budget for the last stages of solar cell fabrication.

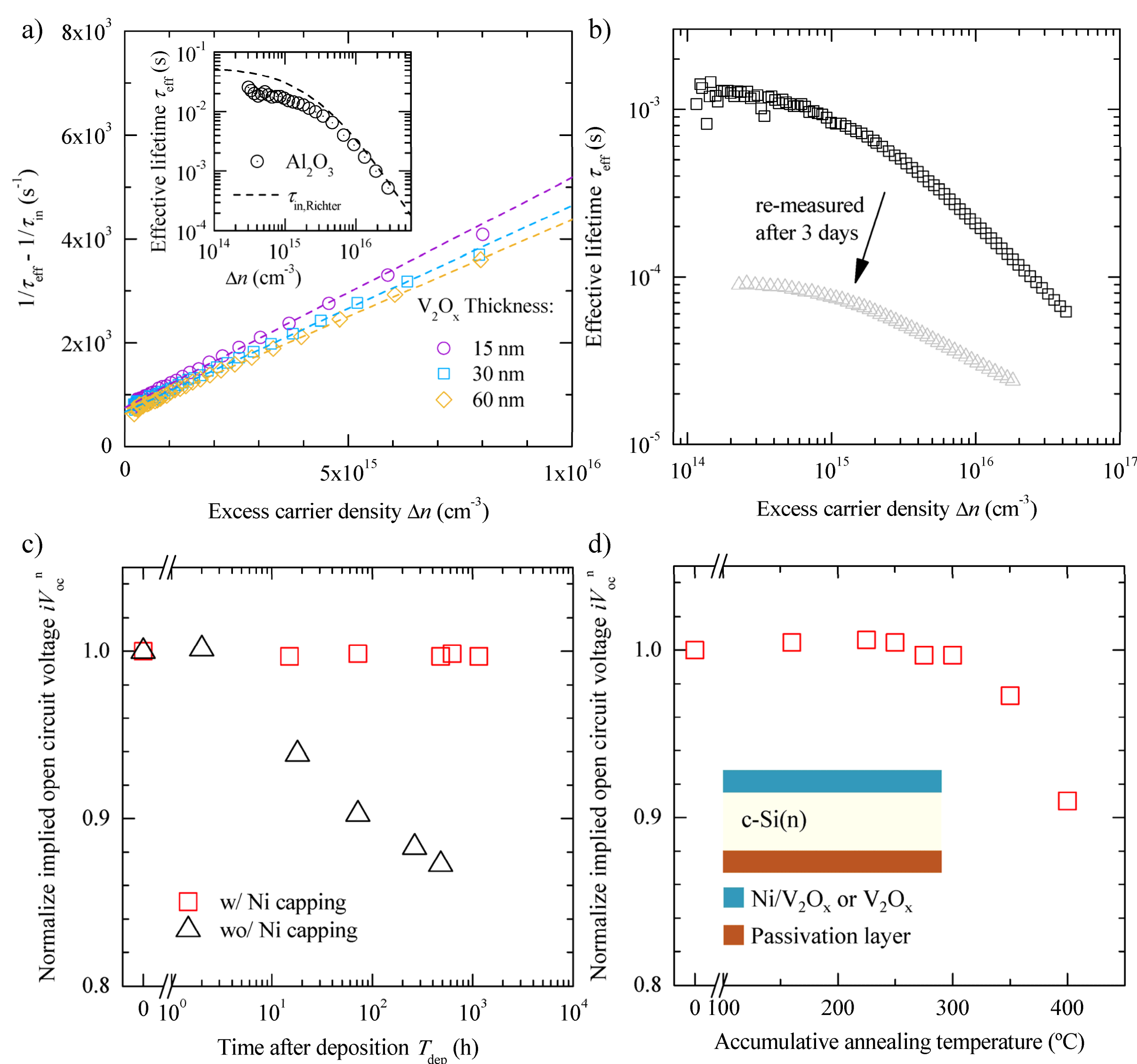

Fig. 1 a) Measured intrinsic-corrected inverse effective lifetime (symbols) and their fitting (dashed line) as a function of the injection level for different V_2O_x thicknesses. Measured τ_{eff} (symbols) and τ_{in} (dashed line) for a symmetrical ALD Al_2O_3 passivated sample is shown in the inset. **b)** Measured τ_{eff} of 40 nm thick V_2O_x layer after its deposition and after three days under air exposure. **c)** Comparative behaviour (time-dependence of iV_{oc} under air exposure) of samples with and without nickel capping. **d)** Effect of the accumulative annealing temperature on the iV_{oc} value. Sketch of passivated samples used in the study is shown in the inset. Notice that in c) and d) the iV_{oc} values are normalized to their initial value.

Please do not adjust margins

To evaluate the electron-blocking and hole-extraction properties, as well as the contact resistance of the V_2O_x layers on c-Si(n) substrates, vertical test diodes were used (fabrication details are in the Experimental section and the test device sketch is depicted on the inset of Fig. 2b). On the one hand, the measured dark current density vs. voltage (*J-V*) curves greatly depends on the metal capping material, nickel or alternatively aluminium, being the former the best choice to contact our devices. The *J-V* curves are enclosed in the ESI† (Fig. S1). We presume that a high ϕ_M value plays a significant role to preserve the high work function of V_2O_x films, which increases the hole-selective contact behaviour. On the other hand, the influence of V_2O_x thickness on the electrical device performance was studied (see Fig. 2a). As it can be seen, the diode ideality factor $n = J/(V_T \times \Delta J/\Delta V)$ (calculated in the middle voltage range and considering a thermal voltage (V_T) of 25.69 mV at 25 °C) improves towards the ideal value, i.e. $n = 1$, as film thickness increases exhibiting a minimum value of ~1.2 for the 40 nm thick V_2O_x sample. Additionally, the specific series resistance (r_s) decreases to 115 mΩcm² as the V_2O_x film thickness increases, obtaining similar results for 40 and 60 nm. Notice that r_s is estimated at forward voltages ~1 V by fitting the real *J-V* characteristic and the ideal one without series resistance.

If the contribution of the rear contacts to the total series resistance is neglected, r_s values are representative of the specific contact resistance between silicon and the Ni/V_2O_x stack as a worst case. Additionally, the expected open circuit voltage ($V_{oc,ex}$) extracted from ideal *J-V* curves without series resistance at a current density of 40 mAcm^{-2}, seems to be limited to 655 ± 5 mV for relatively thick layers (> 30 nm). These values are 20 mV lower than iV_{oc} values obtained from lifetime measurements. This drop might be due to recombination at the rear laser-doped contacts. Finally, an accumulative temperature annealing was done using these test diodes to find the temperature limits of annealing steps after metallization. Fig. 2b shows a rapid degradation with temperatures higher than 150 °C, affecting current transport at high injection voltage levels, i.e. increasing contact resistance.

In order to determine the origin of the good passivation and selective contact, a physical characterization of the V_2O_x/c-Si(n) heterojunction was carried out. Firstly, an X-ray photoelectron spectroscopy (XPS) scan was performed on a 10 nm thick V_2O_x film deposited on a c-Si(n) substrate. Fig. 3a shows the spectra of the vanadium (V 2p) and the oxygen (O 1s) core levels, with both V^{+5} and V^{+4} oxidation states present at their characteristic binding energies,[12] confirming that the V_2O_x film is oxygen deficient and semiconductive in nature. Secondly, a cross-sectional image of the V_2O_x/c-Si(n) interface was obtained via high resolution transmission electron microscopy (HR-TEM), observing the presence of a ~3.5 nm thick amorphous interlayer between the c-Si and the V_2O_x film, Fig. 3b. The formation of such layers has been previously reported for dielectric oxides deposited on c-Si and it has been attributed to the growth of a SiO_x interlayer by chemical reaction.[29,30] We presume this SiO_x interlayer passivates the c-Si surface dangling-bonds, giving rise to the passivating properties of V_2O_x/c-Si heterojunctions. The XPS spectra of the Si 2p core level (see the ESI† Fig. S2) reveals the presence of Si^{+3} oxidation states related to silicon suboxide SiO_x with an oxygen content x ~ 1.5.[31] This would explain why this interfacial layer, amorphous in nature and rich in defect states, is able to conduct even for thicknesses greater than the tunnelling limit (< 2 nm) of fully stoichiometric SiO_2 layers.[32,33] A similar conduction process is assumed for oxygen deficient metal oxides,[8,10] using defect states located within the bandgap as conduction paths for carriers. The valence band spectra measured by XPS (see the ESI† Fig. S3) in the vicinity of the Fermi level (0 eV), shows a characteristic peak at ~2 eV (after subtraction of the H-terminated c-Si component), which is ascribed to the characteristic defect states reported in the literature.[10] Consequently, the continuity of carrier conduction across the c-Si/SiO_x/V_2O_x interfaces can be guaranteed.

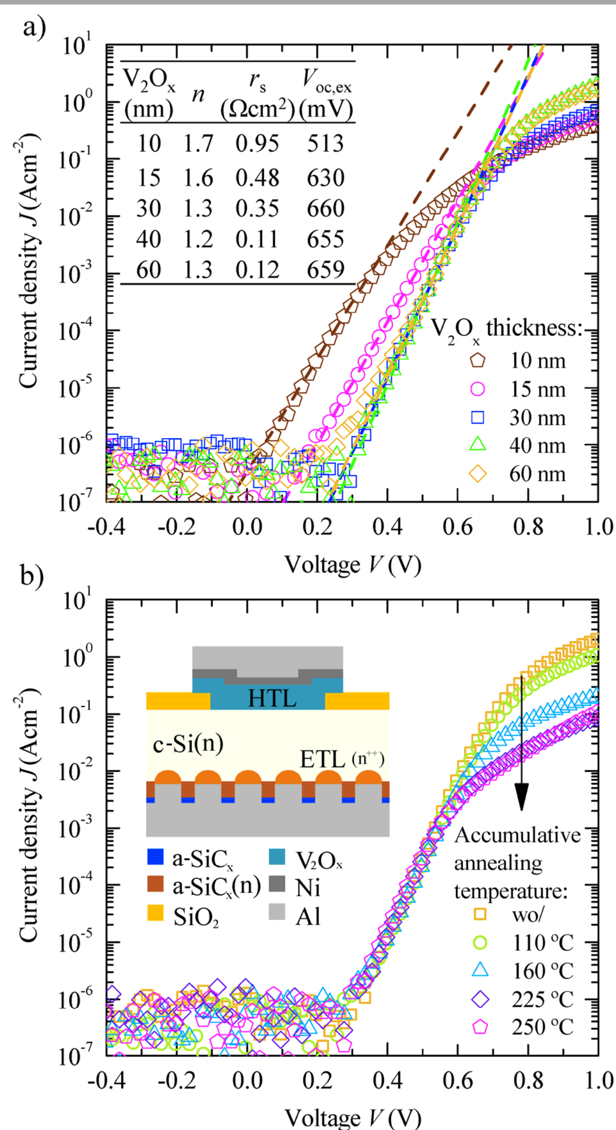

Fig. 2 a) Measured dark *J-V* characteristics for different V_2O_x thicknesses (symbols) and their fitting (dashed line) on c-Si(n) diode test devices. The inside table shows extracted parameters from the test diodes. The r_s and $V_{oc,ex}$ were extracted at 1 V forward voltage and 40 mAcm^{-2} current density, respectively. **b)** Effect of accumulative annealing temperature on the *J-V* characteristic. Sketch of test diodes used in the study is shown in the inset.

This journal is © The Royal Society of Chemistry 20xx

Please do not adjust margins

Please do not adjust margins

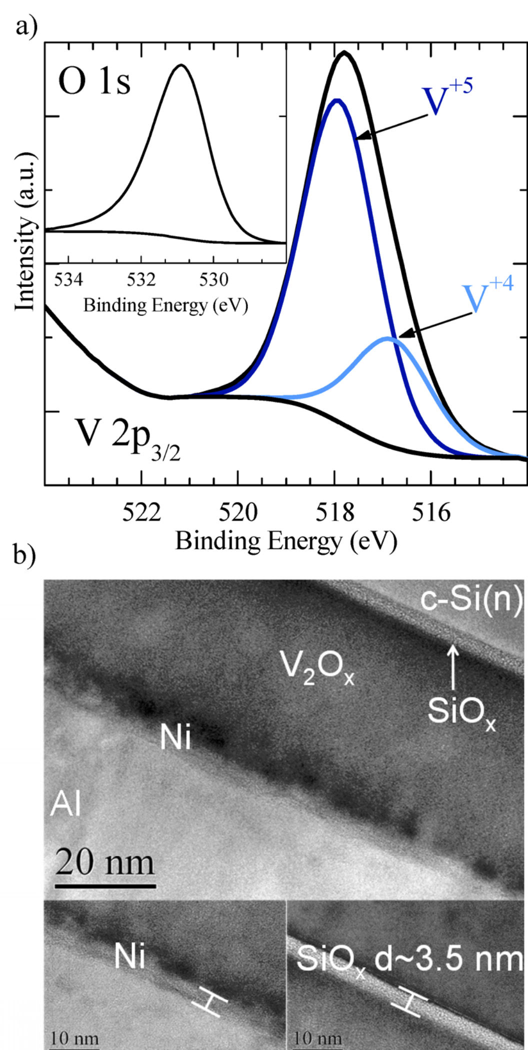

Fig. 3 a) XPS spectra of the V 2p core level, showing V^{+5} and V^{+4} oxidation states. Inset shows the O 1s core level. **b)** HR-TEM image showing a SiO_x interlayer grown on c-Si(n) by a chemical reaction with V_2O_x.

Complementary, the combination of HR-TEM and electron energy loss spectroscopy (EELS) enables obtaining compositional information from the Al/Ni/V_2O_x contact stack (see the ESI† Fig. S4) confirming the presence of the thin uniform Ni capping layer in between aluminium and V_2O_x films.

To demonstrate the applicability of Ni/V_2O_x as a hole contact in IBC solar cells, we fabricated proof-of-concept solar cells (3 x 3 cm^2 area) with different HTL coverage (f_{HTL}), which is defined as the ratio between all HTL regions and the whole device area. A range of f_{HTL} from 40, 52 to 64% was studied in order to know the influence of cell geometry on series resistance and rear surface passivation and its impact on photovoltaic efficiency. Fig. 4a,b depicts the cell schematic structure and the main steps involved in the fabrication process (see Experimental section for details). The fabricated IBC cells combine evaporated V_2O_x films as HTL and DopLa[34,35] (Doped by Laser) ETL regions. Both HTL and ETL strip-like electrodes are defined following an interdigitated pattern isolated from each other with passivated gap regions. Additionally, the metal electrodes contacting each transport layer can be different and optimized for each selective contact thanks to a two-level metallization strategy developed in our devices. In parallel, ALD Al_2O_3 films deposited over random pyramids achieves excellent front surface passivation and very low light reflectance.[24] It is worth to point out that our devices are both free of a-Si:H(i) and TCO materials and avoid high temperature processes, i.e. thermal diffusion and/or thermal oxidation, resulting in a very low thermal budget.

The external quantum efficiency (*EQE*) curves corresponding to the 40, 52 and 64% HTL coverage cells are shown in Fig. 4c. *EQE* values up to 98% in the visible wavelength range confirm the outstanding front surface passivation obtained. The slight influence of f_{HTL} on the *EQE* curves also points out that rear surface passivation provided by both the ETL contacts and the Al_2O_3 layer in the gap between collector regions is sufficient to avoid significant electrical shadowing.[36] Illuminated current density -voltage (*J-V*) curves were measured under standard AM1.5G spectrum (1 kWm^{-2} and T = 25 °C). The photovoltaic parameters are listed in the inset table of Fig. 4d, which also show the *J-V* curve of the best IBC cell efficiency. Conversion efficiencies up to 19.7% were achieved with a short circuit current density (J_{sc}), an open circuit voltage (V_{oc}) and a fill factor (*FF*) of 40.7 mAcm^{-2}, 656 mV and 74.0%, respectively. These results demonstrate that c-Si(n) IBC cells with a Ni/V_2O_x stack as hole-selective contact can reach high efficiencies in a simple low-temperature fabrication process. Notice the high efficiency values reported in this work for solar cells combining both an IBC solar cell architecture and hole transport layers based on transition metal oxides without the use of neither a-Si:H(i) nor TCO's.

Experimental

Test devices. Fabrication and measurements

Test samples and IBC solar cells were fabricated using high quality <100> c-Si(n) float zone (FZ) 4" wafers of 280 ±10 µm thickness and 2 ±1 Ωcm resistivity. Lifetime test samples were cleaned following a RCA1/2 sequence[37] and a diluted HF (1%) dip. Next they were covered with different V_2O_x thicknesses (15, 30 and 60 nm) using Al_2O_3 and silicon carbide carbon-rich layer (a-SiC_x) stack (50 nm/ 35 nm) on the rear side. Effective lifetime measurements use the QSS-PC technique with the WCT-120 instrument (Sinton Consulting).

The test diodes had an active area of 4 × 4 mm^2 patterned on a SiO_2 film grown on c-Si(n) substrate (same as IBC solar cells). V_2O_x films were deposited on the front side and covered with an Al/Ni metal stack (150 nm/ ~5 nm). Several samples were processed considering different V_2O_x thicknesses in the 10 – 60 nm range. In turn, the laser-doped regions (n^{++}), rear point-like contacts were created by irradiating the a-SiC_x(n)/a-SiC_x stack using the same laser system and laser power described next when details of the IBC solar cell process will be given. Consequently, the rear side consists of a square matrix arrangement of point-like contacts with a pitch of 600 µm,

Please do not adjust margins

which corresponds to a contacted fraction area (f_{ETL}) of 0.8%. After the laser-step, the rear side was fully covered with aluminium (1 µm). The electrical measurements were performed under four-contact configuration using an I-V tracer (Keithley 3601B).

The structure of the V_2O_x/c-Si heterojunction was studied with an X-ray photoelectron spectroscopy (XPS) scan performed on a 10 nm thick V_2O_x film deposited on a c-Si(n) substrate, using a non-monochromatic Al-Kα source (1486.6 eV) at $3x10^{-9}$ mbar (SPECS, Phoibos 150 detector). High-resolution TEM (HR-TEM) using a JEOL 2010F with a field emission source (200 kV) determined the microstructural Al/Ni/V_2O_x/c-Si structure. The change in the chemistry was studied by electron energy loss spectroscopy (EELS) technique using a Gatan PEELS system (GIF) in TEM mode. The Al/Ni/V_2O_x/c-Si structure were acquired from cross section lamellas prepared by the focused ion beam (FIB) lift-out technique using a Zeiss 1560XB system.

IBC solar cells. Fabrication and measurements

IBC Solar cells of 3 x 3 cm^2 active area were fabricated as shown in Fig. 4a following the next sequence: the flow process starts with a front side random pyramid texturing by alkaline etching using a tetramethylammonium hydroxide (TMAH) based solution. Next, the wafer was cleaned following a RCA1/2

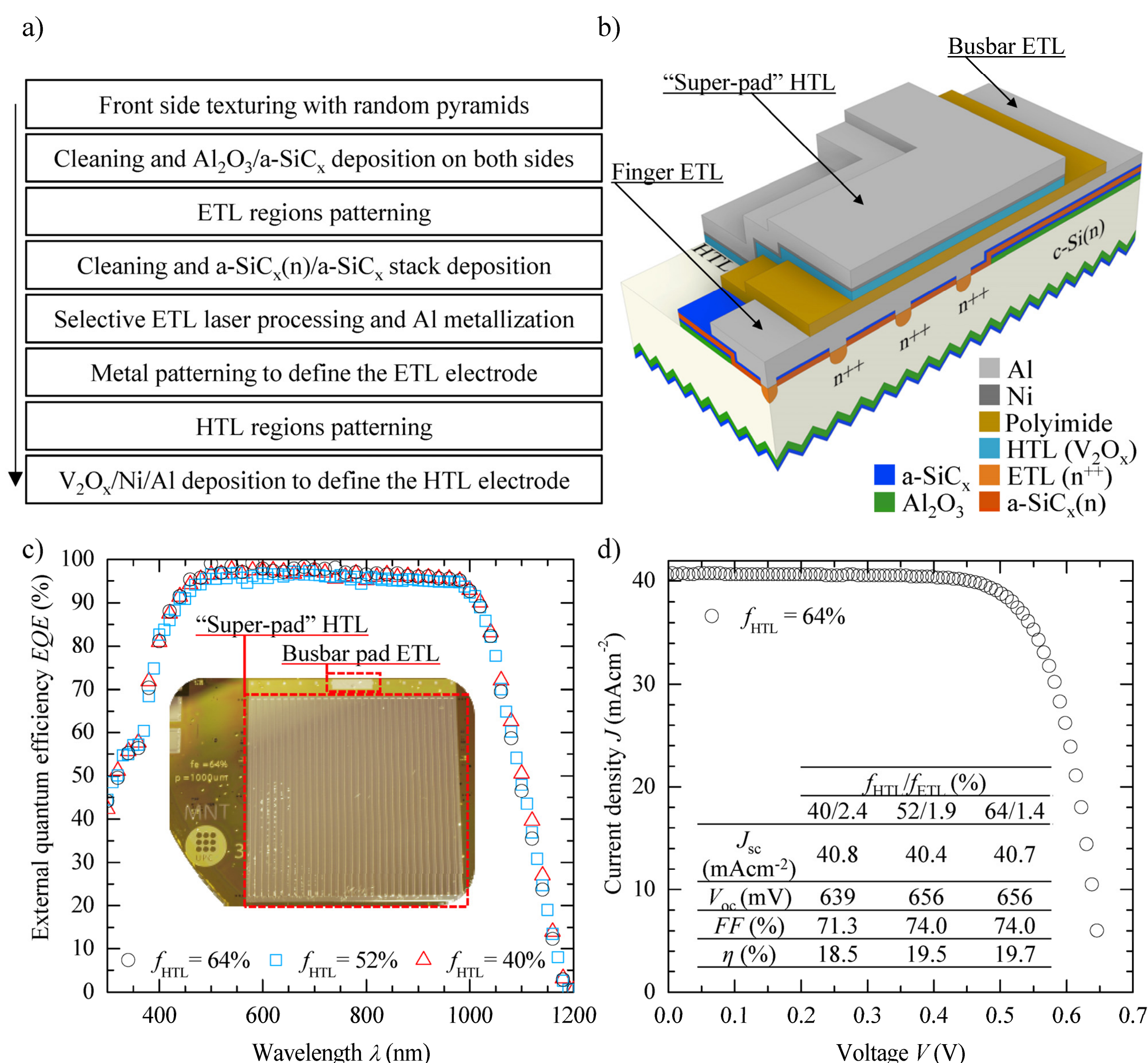

	f_{HTL}/f_{ETL} (%)		
	40/2.4	52/1.9	64/1.4
J_{sc} ($mAcm^{-2}$)	40.8	40.4	40.7
V_{oc} (mV)	639	656	656
FF (%)	71.3	74.0	74.0
η (%)	18.5	19.5	19.7

Fig. 4 a) Process flow showing the main technological steps involved in the fabrication of V_2O_x–based IBC solar cells. **b)** 3D bottom view sketch of the IBC solar cell showing the main layers involved in the structure. Notice that a two-level metallization scheme was used. **c)** *EQE* curves for IBC solar cells with different HTL area coverage f_{HTL}. The image in the inset is a close view of the best solar cell showing the pad through the polyimide layer needed to access the ETL busbar and the top "super-pad" of the HTL electrode. **d)** *J-V* curve for the best IBC solar cells. In the inset there is a summary of the IBC solar cell parameters measured at standard test conditions STC (AM1.5G 1 kWm^{-2} solar spectrum, 25 °C) for the three device topologies with 9 cm^2 active area.

This journal is © The Royal Society of Chemistry 20xx

Please do not adjust margins

Please do not adjust margins

procedure and a 50 nm thick Al_2O_3 layer was deposited on both sides by ALD at 200 °C (Savannah S200, Cambridge Nanotech). Trimethylaluminium (TMA) and water were used as aluminium precursor and oxidant species, respectively. A subsequent 10 min annealing was performed in forming gas (H_2/N_2) at 400 °C in order to activate the surface passivation provided by the Al_2O_3 films.[23,24] Then, a 35 nm thick silicon carbide carbon-rich layer, a-SiC_x ($x \sim 1$), was deposited on both sides to protect the underneath films against subsequent chemical processes. The a-SiC_x layer was deposited by plasma-enhanced chemical vapour deposition (PECVD) process (13.56 MHz, from Electtrorava S.p.A) at a temperature of 300 °C from silane (SiH_4) and methane (CH_4) precursor gases. In order to define the strip-like dielectric regions where point laser contacts will be performed, the a-SiC_x layer was locally removed by dry etching using a tetrafluoromethane (CF_4) plasma process. After a second RCA1 cleaning and a HF (1%) dip, a phosphorous-doped amorphous silicon carbide layer, a-SiC_x(n), and a-SiC_x films was deposited by PECVD (20 nm/ 35 nm). This stack was used as a phosphorous source during the laser doping stage to create point-like ETL regions (n^{++}), as well as to provide a good surface passivation. A lamp-pumped Nd:YAG (StarMark SMP 100II Rofin-Baassel) laser system operating at 1064 nm in the ns regime with 4 kHz pulse repetition frequency and laser power of ~1 W was used to form n^{++} regions.[38] Contacts were arranged at the middle of each ETL finger region with a pitch of 200 µm. Finally, an aluminium (Al) layer (4 µm thick) was thermally evaporated and the interdigitated electrodes were patterned by standard photolithography technique and wet Al etching. Once the ETL laser contacts were done, the whole back surface was covered with a structural photosensitive 5 µm thick polyimide layer,[39] following a two metallization level strategy as seen in Fig. 4b. In this way, the corresponding bottom and top metal materials, Al and Ni/Al respectively, contact ETL and HTL regions. Moreover, the Ni/V_2O_x layers were deposited using a shadow mask, avoiding an additional photolithographic step and simplifying the whole fabrication process. The thick polyimide layer not only avoids any shunting between metal levels but also acts as a protection layer against subsequent dry and wet chemical etchings. After opening a window pad on the HTL regions through the polyimide layer by photolithography, the silicon carbide stack was removed by a CF_4 dry-etching process. Once, a HF (1%) dip etched the Al_2O_3 film a ~40 nm thick V_2O_x film was deposited by thermal evaporation of V_2O_5 powder (Sigma Aldrich, 99.99%) at $8x10^{-6}$ mbar and 0.2 Ås^{-1}. The V_2O_x film was covered by a nickel capping layer (~5 nm) without breaking the vacuum. Finally, a highly conductive Al film (1.5 µm) was evaporated on top of the HTL electrode.

The photovoltaic *J-V* curves and parameters were measured under standard AM1.5G spectrum (1 kW/m^2 and T = 25 °C) using an ORIEL 94021A (Newport) solar simulator. Incident light irradiance was properly calibrated by means of a pyranometer. External quantum efficiency (*EQE*) curves were measured using a commercial instrument (QEX10, PV measurements) with a white light bias of 0.2 Suns and a beam spot of 2 × 2 cm^2 centered within the active device area.

Conclusions

This work has demonstrated a novel dopant free Ni/V_2O_x hole-selective contact and its application to an interdigitated back-contacted c-Si(n) solar cell architecture. Compositional XPS measurements of V_2O_x layers confirm the oxygen deficiency of this material, which might be the origin of conduction states improving carrier transport through the layer. The V_2O_x test structures show saturation current densities J_{0HTL} of 175 fAcm^{-2} and specific contact resistance about 115 mΩcm^2 for 40 nm thick V_2O_x layers. The origin of the good passivation properties, indicated by the relatively low J_{0HTL} an high implied open circuit voltage values (675 mV), is probably due to the presence of a very thin SiO_x interlayer confirmed by TEM measurement. The incorporation of a nickel capping layer over V_2O_x films avoids surface passivation degradation and guarantees the hole-selective contact behaviour. Cell efficiencies of 19.7% in a 9 cm^2 active area are reached with an open circuit voltage of 656 mV, which is a remarkably high value for a Ni/V_2O_x/c-Si(n) heterojunction without additional passivation. These results confirm the interest of transition metal oxides as potential HTL and ETL materials for crystalline silicon solar cells fabricated with lower thermal budgets and simplified processes.

Acknowledgements

This work has been supported partially by the Spanish Government under a FPU grant (FPU13/04381) and through projects TEC2014-59736-R, ENE2013-48629-C4-1-R, ENE2014-56237-C4-2-R and ENE2016-78933-C4-1-R. Part of the work is also supported by the project REFER COMRDI15-1-0036 ACCIÓ and European Regional Development Fund (FEDER). P.O. acknowledges financial support from the project ENE2013-49984-EXP of the Spanish Ministry of Economy and Competitiveness (MINECO) and L.G.G acknowledges financial support from Mexico's national grant program CONACyT.

References

1 K. Yoshikawa, H. Kawasaki, W. Yoshida, T. Irie, K. Konishi, K. Nakano, T. Uto, D. Adachi, M. Kanematsu, H. Uzu and K. Yamamoto, *Nat. Energy*, 2017, **2**, 17032.
2 M. D. Lammert and R. J. Schwartz, *IEEE Transactions on Electron Devices*, 1977, **24**, 337.
3 U. Würfel, A. Cuevas and P. Würfel, *IEEE J. Photovoltaics*, 2015, **5**, 461.
4 C. Battaglia, A. Cuevas and S. De Wolf, *Energy Environ. Sci.*, 2016, **9**, 1552.
5 T.-G. Chen, B.-Y. Huang, E.-C. Chen, P. Yu and H.-F. Meng, *Appl. Phys. Lett.*, 2012, **101**, 033301.
6 Y. Zhang, R. Liu, S.-T. Lee and B. Sun, *Appl. Phys. Lett.*, 2014, **104**, 083514.
7 C. Battaglia, X. Yin, M. Zheng, I. D. Sharp, T. Chen, S. McDonnell, A. Azcatl, C. Carraro, B. Ma, R. Maboudian, R. M. Wallace and A. Javey, *Nano Lett.*, 2014, **14**, 967.
8 M. T. Greiner, M. G. Helander, W.-M. Tang, Z.-B. Wang, J. Qiu and Z.-H. Lu, *Nature Mat.*, 2011, **11**, 76.
9 J. Meyer, S. Hamwi, M. Kröger, W. Kowalsky, T. Riedl and A. Kahn, Adv. Mater., 2012, **24**, 5408.
10 M. T. Greiner and Z. H. Lu, *NPG Asia Mater.*, 2013, **5**, e55.

This journal is © The Royal Society of Chemistry 20xx

Please do not adjust margins

Please do not adjust margins

11 J. Bullock, A. Cuevas, T. Allen and C. Battaglia, *Appl. Phys. Lett.*, 2014, **105**, 232109.
12 L. G. Gerling, S. Mahato, A. Morales-Vilches, G. Masmitjà, P. Ortega, C. Voz, R. Alcubilla and J. Puigdollers, *Solar Energy Mater. Solar Cells*, 2016, **145**, 109.
13 C. Battaglia, S. M. Nicolás, S. Wolf, X. Yin, M. Zheng, C. Ballif and A. Javey, *Appl. Phys. Lett.*, 2014, **104**, 113902.
14 J. Bullock, M. Hettick, J. Geissbühler, A. J. Ong, T. Allen, C. M. Sutter-Fella, T. Chen, H. Ota, E. W. Schaler, S. De Wolf, C. Ballif, A. Cuevas and A. Javey, *Nat. Energy*, 2016, **1**, 15031.
15 J. Geissbühler, J. Werner, S. M. Nicolas, L. Barraud, A. Hessler-Wyser, M. Despeisse, S. Nicolay, A. Tomasi, B. Niesen, S. De Wolf and C. Ballif, *Appl. Phys. Lett.*, 2015, **107**, 081601.
16 J. Bullock, C. Samundsett, A. Cuevas, D. Yan, Y. Wan and T. Allen, *IEEE J. Photovoltaics,* 2015, **5**, 1591.
17 M. Bivour, J. Temmler, F. Zähringer, S. Glunz and M. Hermle, presented at the *43rd IEEE Photovoltaic Specialists Conf. (PVSEC)*, Portland, 2016.
18 H.-D. Um, N. Kim, K. Lee, I. Hwang, J. H. Seo and K. Seo, *Nano Lett.*, 2016, **16**, 981.
19 W. Wu, J. Bao, X. Jia, Z. Liu, L. Cai, B. Liu, J. Song and H. Shen, *Phys. Status Solidi RRL*, 2016, **10**, 662.
20 Z. C. Holman, A. Descoeudres, L. Barraud, F. Z. Fernandez, J. P. Seif, S. De Wolf and C. Ballif, *IEEE J. Photovoltaics,* 2012, **2**, 7.
21 B. Demaurex, S. De Wolf, A. D. Descoeudres, Z. C. Holman and C. Ballif, *Appl. Phys. Lett.*, 2012, **101**, 171604.
22 R. A. Sinton, A. Cuevas and M. Stuckings, presented at the *25th IEEE Photovoltaic Specialists Conf. (PVSC)*, Washington DC, 1996.
23 B. Hoex, J. Schmidt, P. Pohl, M. C. M. Van de Sanden and W. M. M. Kessels, *J. Appl. Phys.*, 2008, **104**, 044903.
24 G. López, P. Ortega, C. Voz, I. Martín, M. Colina, A. B. Morales, A. Orpella and R. Alcubilla, *Beilstein J. Nanotechnol.*, 2013, **4**, 726.
25 I. Martín, M. Colina, A. Coll, G. López, P. Ortega, A. Orpella and R. Alcubilla, *Energy Procedia*, 2014, **55**, 255.
26 A. Richter, S. W. Glunz, F. Werner, J. Schmidt and A. Cuevas, *Phys. Rev. B*, 2012, **86**, 165202.
27 M. C. Gwinner, R. Di Pietro, Y. Vaynzof, K. J. Greenberg, P. K. H. Ho, R. H. Friend and H. Sirringhaus, *Adv. Funct. Mater.,* 2011, **21**, 1432.
28 J. Meyer, K. Zilberberg, T. Riedl and A. Kahn, *J. Appl. Phys.,* 2011, **110**, 033710.
29 G. D. Wilk, R. M. Wallace and J. M. Anthony, *J. Appl. Phys.*, 2001, **89**, 5243.
30 L. G. Gerling, C. Voz, R. Alcubilla and J. Puigdollers, *J. Mater. Research*, 2017, **32**, 260.
31 F. J. Himpsel, F. R. McFeely, A. Taleb-Ibrahimi and J. A. Yarmoff, *Phys. Rev. B.,* 1988, **38**, 6084.
32 J. Schewchun, R. Singh and M. Green, J*. Appl. Phys.*, 1977, **48**, 765.
33 M. A. Green, *Appl. Phys. Lett.*, 1978, **33**, 178.
34 I. Martín, J. M. López-González, M. Colina, A. Orpella and R. Alcubilla, presented at the *28th European Photovoltaic Solar Energy Conf. (EU PVSEC)*, Paris, 2013.
35 G. López, P. Ortega, I. Martín, C. Voz, A. Orpella and R. Alcubilla, *Energy Procedia,* 2016, **92**, 652.
36 C. Reichel, F. Graneck, M. Hermle and S. W. Glunz, *Prog. Photovolt: Res. Appl.*, 2013, **21**, 1063.
37 W. Kern, *J. Electrochem. Soc.*, 1990, **137**, 1887.
38 G. López, P. Ortega, M. Colina, C. Voz, I. Martín, A. Morales-Vilches, A. Orpella and R. Alcubilla, *Appl. Surf. Science*, 2015, **336**, 182.
39 Fujifilm Electronic Materials, Photosensitive – Solvent Developable Polyimides: Durimide® 7505 type, http://www.fujifilm-ffem.com, accessed September 2016.

This journal is © The Royal Society of Chemistry 20xx

Please do not adjust margins